Nuclear Engineering and Design 380 (2021) 111328

Contents lists available at ScienceDirect

Nuclear Engineering and Design

journal homepage: www.elsevier.com/locate/nucengdes

Evaluation of ASR in concrete using acoustic emission and deep learning

Li Ai [a], Vafa Soltangharaei [a,*], Paul Ziehl [b]

[a] Department of Civil and Environmental Engineering, University of South Carolina, 300 Main Street, Columbia, SC, USA
[b] College of Engineering and Computing, Swearingen Engineering Center, 301 Main Street, Suite 3A41, Columbia, SC, USA

A B S T R A C T

Alkali-silica reaction (ASR) is one of main damages causes in concrete structures such as nuclear power plants which may endanger structural serviceability and integrity. Acoustic emission (AE) is a passive nondestructive method for structural health monitoring. It is very sensitive and has the capability of monitoring structures continuously. This method may be an alternative for early damage detection in concrete nuclear structures affected by ASR. The innovation of this paper lies in the implementation of deep learning algorithms to evaluate the ASR progress. ASR was monitored by AE in a concrete specimen, which was cast with reactive coarse aggregates and reinforced by steel rebars. The AE signals recorded during the experiment were filtered and divided into two classes. Two deep learning algorithms of convolutional neural network (CNN) and stacked autoencoder were employed to classify the AE signals into the corresponding classes. The model based on CNN resulted in a classifier with higher accuracy than the model based on the autoencoder network.

1. Introduction

Concrete is one of the important infrastructure materials which is wildly applied in civil engineering structures. However, the brittle mechanical property of concrete makes it vulnerable to cracking. ASR is one of the main sources of cracking in concrete structures. ASR is a chemical reaction between silica in reactive aggregate and alkaline ions in cement. The product of this reaction is a hygroscopic gel, which absorbs humidity and expands (Soltangharaei et al., 2018b). The gel exerts pressure on the aggregate and cement matrix, and causes cracking. The common structures, which are exposed to ASR are bridges (Bach et al., 1993; Bakker, 2008; Clark, 1989; Schmidt et al., 2014), concrete dams (Campos et al., 2018; Plusquellec et al., 2018), nuclear power plants, and nuclear waste containments (Saouma and Hariri-Ardebili, 2014; Soltangharaei et al., 2018a; Takakura et al., 2005; Tcherner and Aziz, 2009). Because of the safety and radioprotection functions of concrete structures in nuclear power plant, the effects of ASR to current and long-term operations must be thoroughly addressed.

Many approaches were applied to monitor ASR damage and evaluate its effect on structures. The conventional approaches include regular-base visual inspection, coring and petrographic analysis, demountable mechanical strain gauge (DEMEC gauge), relative humidity or moisture content measurement, and crack indexing. These approaches have several disadvantages. For example, visual inspection is usually not effective for the early detection of ASR damage. Generally, due to in-plane constraints of structures, the surface cracks appear in a late stage of ASR process, and the visual inspection of large-scale structures is time-consuming and prone to human error (Rajabipour et al., 2015). Coring and petrographic analyses are destructive methods that are generally not suitable for sensitive structures such as nuclear power plants. Furthermore, it is difficult to evaluate the condition of entire structure with only a few cores or samples.

AE can be an alternative for the temporal evaluation of ASR damage in concrete structures used in nuclear facilities. This method is sensitive and has a continuous monitoring capability (Anay et al., 2020, 2018; Assi et al., 2018; Li et al., 2017; Ono, 2011; Soltangharaei et al., 2020a, 2020b). Recently, there have been several investigations conducted where AE was applied for the detection of damage and the quantification of the defects caused by ASR (Abdelrahman et al., 2015; Ai et al., 2021a; Farnam et al., 2015; Lokajíček et al., 2017; Soltangharaei et al., 2020a, 2018b; Weise et al., 2012). Farnam et al. (2015) utilized peak frequency and frequency centroid to characterize signal signatures that emanate from cracks in aggregates and cement paste. High-frequency signals were observed in the earlier stage of ASR, while the low-frequency signals appeared later in the ASR process. X-ray images helped the authors to verify their hypothesis. Lokajíček et al. (2017) utilized both ultrasonic pulse velocity and AE to monitor the damage caused by ASR. Four specimens with different aggregate reactivities were used. The selection of the appropriate features was generally based on experience and very challenging especially for complex data sets. Therefore, an automatic approach is required to extract features directly from raw data and find potential patterns in the complex data sets. This goal can be fulfilled by using deep learning methods.

Deep learning is one of the artificial intelligence techniques that

* Corresponding author.
E-mail addresses: ail@email.sc.edu (L. Ai), vafa@email.sc.edu (V. Soltangharaei), Ziehl@cec.sc.edu (P. Ziehl).

https://doi.org/10.1016/j.nucengdes.2021.111328
Received 15 October 2020; Received in revised form 31 March 2021; Accepted 3 June 2021
Available online 15 June 2021

simulates information processing in the human brain (Goodfellow et al., 2016; Ruixiao Sun et al., 2021). The advantage of deep learning is using raw data instead of extracted features as an input set. Therefore, there is no need for feature extraction and feature selection, which can be challenging for complex data sets (Sadoughi et al., 2018). CNN is one of the state-of-art deep learning algorithms (Guo et al., 2021; Khan et al., 2020; Redmon and Farhadi, 2018; Ren et al., 2016), which develops rapidly, and is widely studied in image recognition and target detection. Ren et al. (2017) proposed a faster R-CNN (Region-based CNN). This new target detection model presented a Region Proposal Network (RPN) based on a Fast R-CNN, which significantly increases the efficiency of target detection. Redmon et al. (2018) proposed Yolov3 as an improved architecture of Yolo network. This improved architecture has higher accuracy, and training speed is acceptable. In addition to design a deeper architecture of CNN, using a hybrid method is another strategy to improve the performance of CNN (Kim and Cho, 2019; Niu and Suen, 2012). Niu et al. (2012) presented a hybrid model based on CNN and Support Vector Machine (SVM) to recognize the handwriting digits. In the hybrid model, the convolutional layers extract features, and the SVM works as a recognizer. The results indicated that this fusion could obtain better accuracy than a single model. Kim et al. (2019) proposed a hybrid model for the prediction of residential energy consumption. The hybrid model consisted of CNN and a long short-term memory network (LSTM). The convolutional layers could extract features from complex variables that affected energy consumption. The LSTM layers were designed to model the temporal information of irregular trends in time series components. Compared with the previous work, a better performance was observed by using the proposed hybrid model.

In recent years, deep learning has been applied in AE (Ai et al., 2021b; Ebrahimkhanlou et al., 2019; Li et al., 2020; Shevchik et al., 2018). Ai et al. (2021b) developed a passive nondestructive health monitoring system to locate impacts on an aircraft component based on AE and deep learning. An autoencoder algorithm was trained by the data and utilized as a part of the health monitoring system. Ebrahimkhanlou et al. (2019) worked on a deep learning framework based on a stacked autoencoder network to locate AE events on the metal structures. Li et al. (2020) utilized a convolutional neural network for AE wave classification to obtain a more accurate and comprehensive rail crack monitoring in the field with complex cracking conditions, high-operational noise, and large data. Shevchik et al. (2018) proposed an on-site quality monitoring system for additive manufacturing by utilizing AE and a spectral convolutional neural network.

The main focus of this paper is to relate AE data collected during ASR process and attribute them to ASR expansion strains. CNN and autoencoder networks were used to develop data-driven models and relate raw data to classes, which were corresponding to strain ranges. Using this method, sensitive structures such as nuclear power plants or waste containments can be continuously monitored for ASR cracking without interrupting the structural serviceability and destructing the structures. Furthermore, ASR process phases can be determined using a developed data-driven model. The authors are currently not aware of any published similar works that implement a deep learning algorithm to relate AE data to ASR expansion strains.

2. Test setup and experimental procedure

A concrete block specimen with the dimensions of the 305 mm × 305 mm × 1120 mm was prepared for ASR testing. The specimen was cast with reactive coarse aggregates and reinforced by steel rebars. The geometric of the specimen is shown in Fig. 1a. The detail of the reinforcements is presented in Fig. 1b. The specimen had four longitudinal US #7 steel rebars and transversal US #6 steel rebars with 150 mm spacing. All rebars were T-headed to compensate for the short development length.

Ten AE sensors were attached to the surfaces of the specimen using grey double/bubble epoxy. The sensor layout is presented in Fig. 1a (Soltangharaei et al., 2020a). Three sensors (sensor 8–10) were attached to the front longitudinal side surface. Three sensors (sensor 5–7) were attached on the back longitudinal side surface. Two sensors (sensor 1–2) were attached on the top, while sensors 3–4 were attached to the bottom surface. The sensors were PKWDI with an operating frequency of 200–850 kHz. AE signals were acquired by a 24-channel Micro-II Express data acquisition system manufactured by MISTRAS Group, Inc. (Princeton Junction, NJ, USA). The sampling rate was set to 5 MHz.

A chamber with the dimensions of 243 cm (width) × 243 cm (length) × 122 cm (height) was designed and built to accelerate the ASR process by providing high temperature and humidity. The temperature inside the chamber was kept at 37 ± 3 °C. The humidity was kept around 95% ± 5%. The specimen was placed on a steel carrier with wheels, which was designed and fabricated as the support of the specimen. DEMEC gauges were used for the expansion measurement by measuring the distance between pins (Fig. 1a) along three dimensions. The expansion was measured regularly every month, and the maintenance of AE sensors was conducted at the same time to ensure the bonding status between sensors and specimen. More details about the test setup and procedures can be found in (Soltangharaei et al., 2020a).

3. Analysis procedure

In this paper, two methods based on deep learning were proposed to evaluate ASR in concrete. One is based on continuous wavelet transforms (CWT) and CNN. The other one is based on a stacked autoencoder network. The AE signals are divided into two subsets according to the temporal evolution of signal features. Each subset of data can be attributed to an ASR expansion range. The data-driven models are developed using CNNs and stacked autoencoders to attribute the AE signals to the corresponding subsets.

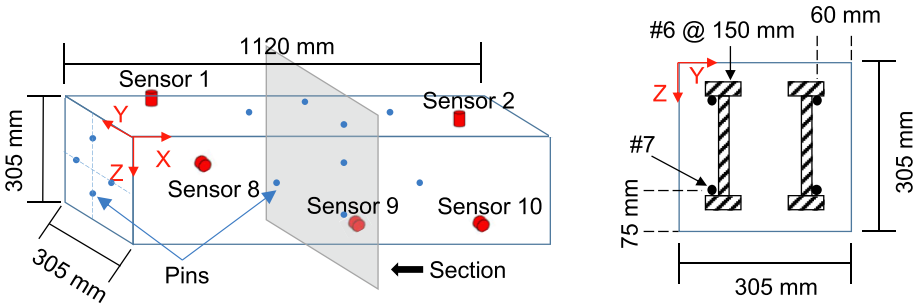

(a) Concrete specimen (b) Reinforcement detail

Fig. 1. Structural details of specimen.

3.1. Continuous wavelet transform

CWT is a joint time–frequency analysis method that captures the time–frequency characteristics in non-stationary signals such as AE signals (Gou et al., 2020). CWT has a good performance in signal processing in terms of both time and frequency (Li et al., 2018). The continuous wavelet coefficients can be expressed by a scalogram image. The 2D scalogram images are the input for CNN models. In this paper, the Morse wavelet is selected as the mother wavelet function to conduct CWT. The Fourier transform of Morse wavelet is presented in Eq (1):

$$\Psi_{p,\gamma}(x) = U(x)\alpha_{p,\gamma}x^{\frac{p^2}{\gamma}}e^{-x^{\gamma}} \quad (1)$$

where $U(x)$refers to the unit step, $\alpha_{p,\gamma}$ refers to the normalizing constant, p^2 refers to the time-bandwidth product.γ is the parameter that characterizes the symmetry of the Morse wavelet (Lilly and Olhede, 2008). In this paper, p^2 and γ was defined as 60 and 3.

3.2. Convolutional neural network

CNN is a deep neural network with convolutional filters (Krizhevsky et al., 2012). CNN is generally composed of three main parts: an input layer, feature extraction layers, and a fully connected layer. The core part of the feature extraction layers mainly includes convolutional layers and pooling layers. The architecture of a typical CNN with two convolutional layers and two pooling layers is shown in Fig. 2.

In the convolutional layer, multiple convolutional kernels are employed to filter the input and generate feature maps. The pooling layer is used for the down-sampling of feature maps obtained from the previous convolutional layer (Yongyi Sun et al., 2020). If the image feature maps are directly used for classification without any processing, a great computational complexity will be generated, and the model is prone to overfitting. Therefore, a further reduction in the dimensionality of feature maps is required, which is the reason to construct the pooling layer after each convolutional layer. The fully connected layer is employed at the end of the CNN model. It converts the feature maps, resulting from the previous pooling layer, to one feature vector.

GoogLeNet is an architecture of CNN that developed based on the LeNet model (Szegedy et al., 2015). The number of layers is extended up to 22. The GoogLeNet model is pre-trained by more than a million images from a subset of ImageNet database (Deng et al., 2009). GoogLeNet has been reported to have a good performance for the identification of acoustic emission signals in the scenarios such as the monitoring of wear in sliding bearing system (König et al., 2021a, 2021b) and the monitoring of stay cable in a bridge (Xin et al., 2020). Therefore, GoogLeNet was selected in this paper as a preliminary study of applying CNN to evaluate concrete ASR expansion.

In this paper, the input data is 2D wavelet images. Before input datasets, the data is labeled and normalized. The wavelet coefficients are scaled between 0 and 1.

3.3. Stacked autoencoder

The stacked autoencoder is also employed to classify the data, and the results are compared to CNN. The stacked autoencoder neural network is a deep neural network composed of multiple autoencoders (Bengio et al., 2007). An autoencoder is a neural network usually with three layers. The number of neurons in the input and output layers is the same. The algorithm condenses the input data according to the dimension of the hidden layer and reconstructs the output of condensed data to the output layer (Ng and Autoencoder, 2011). An objective function is designed to minimize the error in input data and output data. The compression process of input data can be considered as the feature extraction process. In stacked multiple autoencoders, more than one autoencoder is utilized to condense the data. In other words, the data is condensed several times by multiple autoencoders. A SoftMax layer is connected to the last autoencoder to classify final compressed features. In this paper, a stacked autoencoder with two autoencoders is employed. The input data is the Fast Fourier Transforms (FFT) magnitude of the AE waveforms. In other words, the input data set includes a matrix with rows representing the number of signals and columns representing FFT magnitudes of signals. The first and second autoencoder has a size of 100 and 50 neurons, respectively. Fig. 3 illustrates the structure of the stacked autoencoder network used in this paper.

4. Results and discussion

4.1. Analysis of features and class definition

The AE data acquired from the sensors during ASR have been utilized for analysis. Some sensors collected a large amount of extraneous data due to faulty connections and environmental noise. Therefore, the first step before analyzing the AE data is filtering. The noises from faulty connections have specific signal features such as small counts, average frequency, and peak frequency. Initially, the noises related to the faulty connections were removed by deleting the data with an average frequency lower than 60 kHz. Some faulty data remained from the first stage. Therefore, another filter was applied to the contaminated channel by removing the signals with a peak frequency of less than 80 kHz. The filtering procedure mentioned above removed a large amount of faulty data. Then, a procedure was developed to further filter the data based on AE event definition. An AE event refers to a set of hits acquired by different sensors in a specific time interval, which is defined based on a stress wave velocity and specimen dimensions. Only the events which include at least four hits were considered valid data and kept, and the rest of the data was considered as noise and was therefore deleted.

Several AE features were extracted from the AE signals after filtering. Those features can be divided into non-frequency-based features and frequency-based features. The non-frequency-based features in this paper are counts, counts to peak, amplitude, rise time, duration, and signal strength. The non-frequency-based features are presented for a typical AE waveform, as shown in Fig. 4a.

To extract the frequency-based features, the AE signals were

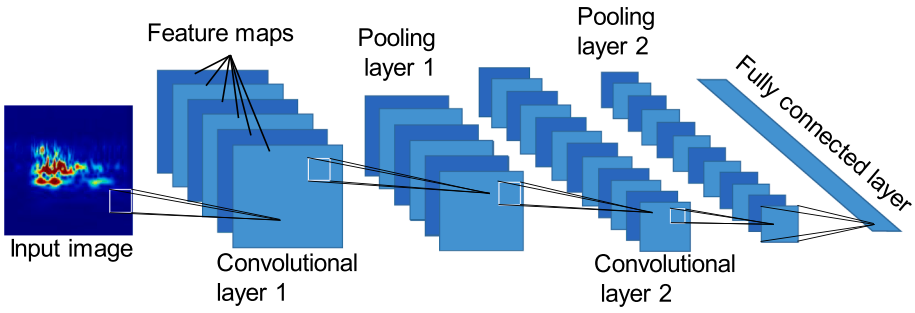

Fig. 2. Architecture of a typical CNN.

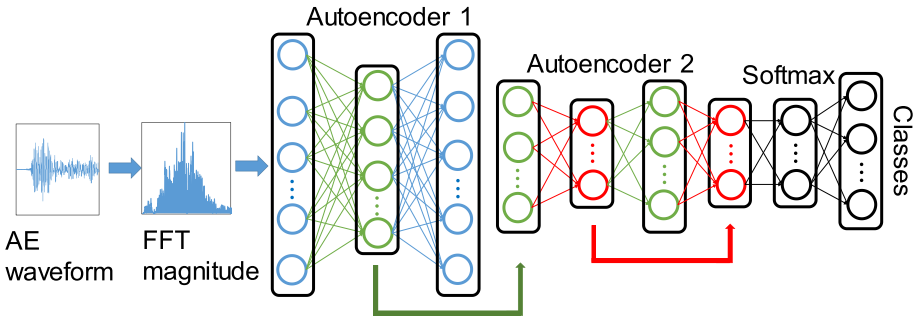

Fig. 3. A stacked autoencoder composed of two autoencoders.

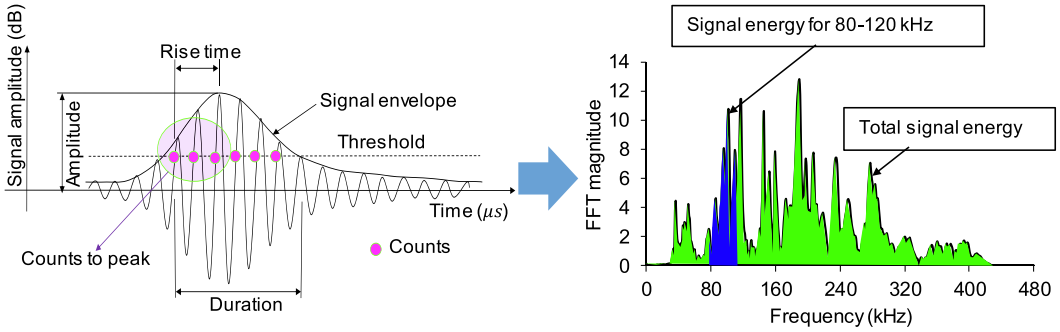

(a) Non-frequency-based feature extraction

(b) Frequency-based feature extraction for 80-120 kHz

Fig. 4. AE features.

transferred to the frequency domain using FFT. The frequency domain of each signal was divided by ten equal intervals with a bandwidth of 40 kHz. The energies corresponding to each frequency band were derived by calculating the area under the FFT spectrum in that frequency band (Fig. 4b). The energies in the frequency bands were normalized to the total energy of the signal, which was calculated by the area under the entire FFT spectrum (Fig. 4b). These normalized energies for different frequency bands are referred to as frequency-based features in this paper. Fig. 4b shows the extraction of frequency-based features in the range of 80–120 kHz.

The average temporal evolution of some features such as counts, counts to peak, amplitude, signal strength, signal energy for 0–40 kHz, and signal energy for 80–120 kHz are illustrated in Fig. 5. All the features were normalized to 0–1. The features shown in Fig. 5 indicate the change in the temporal evolution at almost the same time, around 190 to 200 days. The ASR process can be divided into two phases (phase 1 and phase 2) according to the observed trend.

The signal amplitudes and the cumulative signal strength (CSS) for the concrete specimen are presented in Fig. 6a. The jumps in the cumulative signal strength curve are representative of a new crack initiation event or a crack extension along an existing crack. The major jump occurs around 200 days, which coincides with the time related to change in the AE features shown in Fig. 6. Therefore, day 190 was employed to divide the ASR process into the first and second phases. The phase definition is deployed as the label of AE signals in the deep learning models. The models will classify the input AE signals into two classes according to the phase definition (phase 1 and phase 2).

The strain measurements were conducted along different dimensions on the specimen surfaces during ASR. The volumetric strain is defined as the accumulation of average strains along the X, Y, and Z axes. Results of the volumetric strain range are presented in Fig. 6b. In phase 1, the strain range changes from 0% to 20%, and in phase 2, the strain range changes from 20% to 55%.

4.2. Waveforms and CWT images

There are 1668 and 1402 AE signals in classes 1 and 2, respectively. The input set for the stacked autoencoder was FFT spectra of AE signals. The other data set was prepared by conducting CWT on the data. The coefficients of CWTs were saved as 2D contour images, and the images were utilized as an input data set for CNN. Both deep learning models (autoencoder and CNNs) classify the AE signals into the attributed classes. A time-domain waveform and its FFT spectrum are randomly selected for each class and presented in Fig. 7. Moreover, the CWT images of the signals are presented in Fig. 8. The amplitudes of AE waveforms were normalized to a range of − 1 to 1. The frequency-domain waveforms were normalized by the maximum magnitudes, and the wavelet coefficients were scaled between 0 and 1.

4.3. Evaluation of ASR data using CNN

4.3.1. Classification using all AE signals

From all CWT contour images, 70% of images were randomly selected for a training set of CNN, and 30% of images were randomly selected for a validation set. The designated phases (phase 1 or 2) of the AE signals were utilized as data labels. The classification result of the validation dataset is presented in the confusion matrix (Fig. 9a). Among the CWT images in phase 1, 74.6% of images were correctly classified as phase 1, while 25.4% of images were classified as phase 2. Among the images in phase 2, 80.2% of them were correctly classified, while 19.8% of images were misclassified as phase 1. In total, 707 images were correctly classified to the corresponding phases, which was 76.7% of all images in the validation data set. In other words, the accuracy of the CNN classifier is 76.7% (Fig. 9a). Precision and recall are employed as parameters to evaluate the classification performance in each phase. Generally, precision can be calculated by Eq. (2):

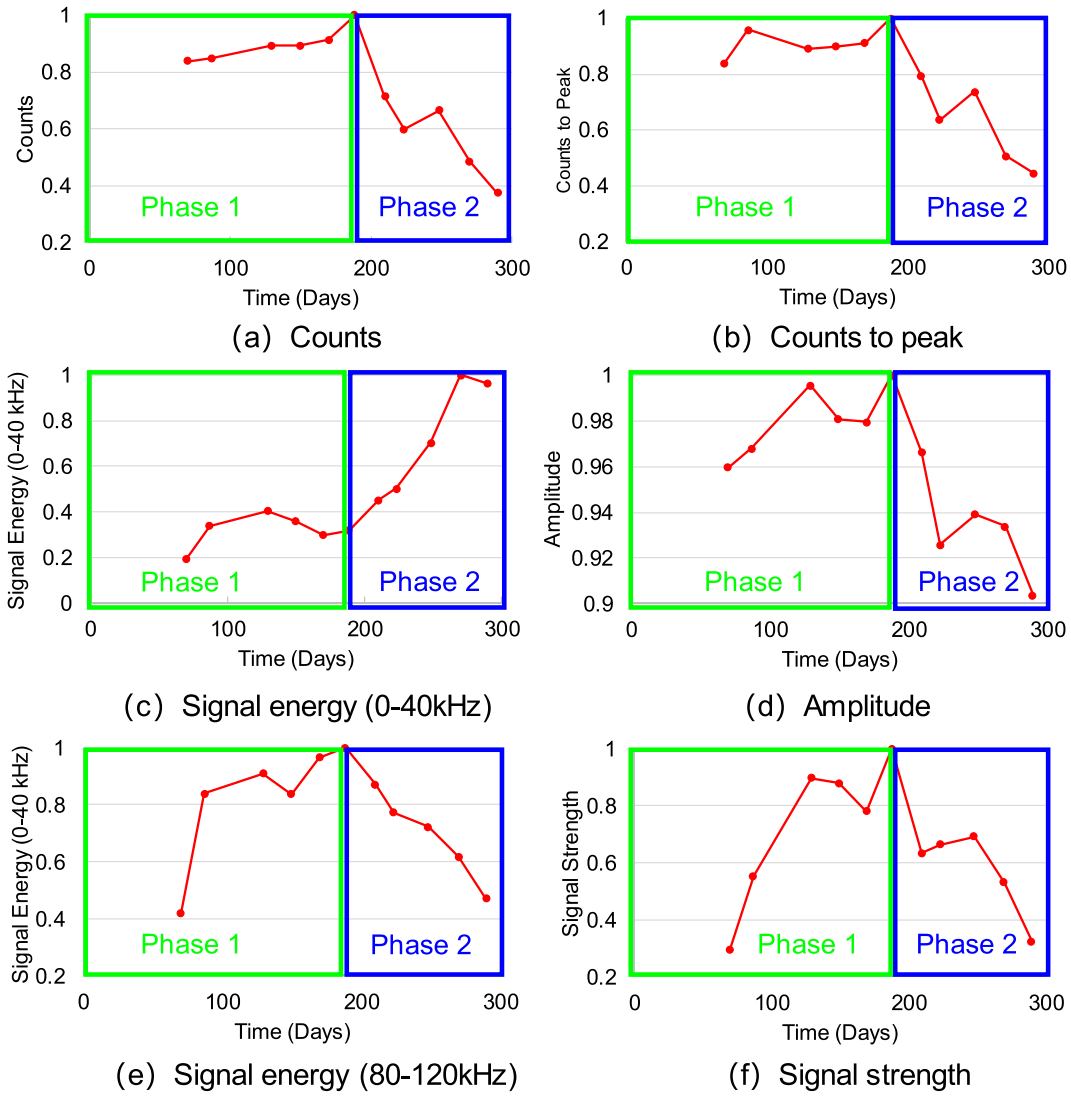

Fig. 5. Temporal evolution of AE features during ASR process.

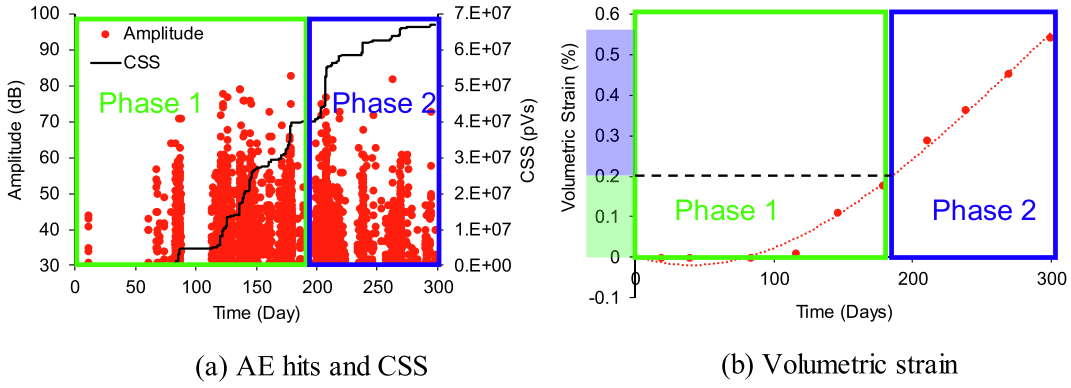

Fig. 6. AE amplitudes and volumetric strain presentations with designated classes.

$$Precision = \frac{TP}{TP + FP} \tag{2}$$

where, *TP*, is the true positive, which refers to the number of samples correctly classified to the attributed class. *FP* is the false positive, which refers to the number of samples that do not belong to the class and are misclassified into the class. The precisions of CNN model using all AE data for classes 1 and 2 are 85.5% and 66.8%, respectively (Fig. 9a).

The recall parameter can be calculated as follows:

$$Recall = \frac{TP}{TP + FN} \tag{3}$$

where *FN* is the false negative, which is the number of samples that belong to a class but are misclassified as other classes. The recall

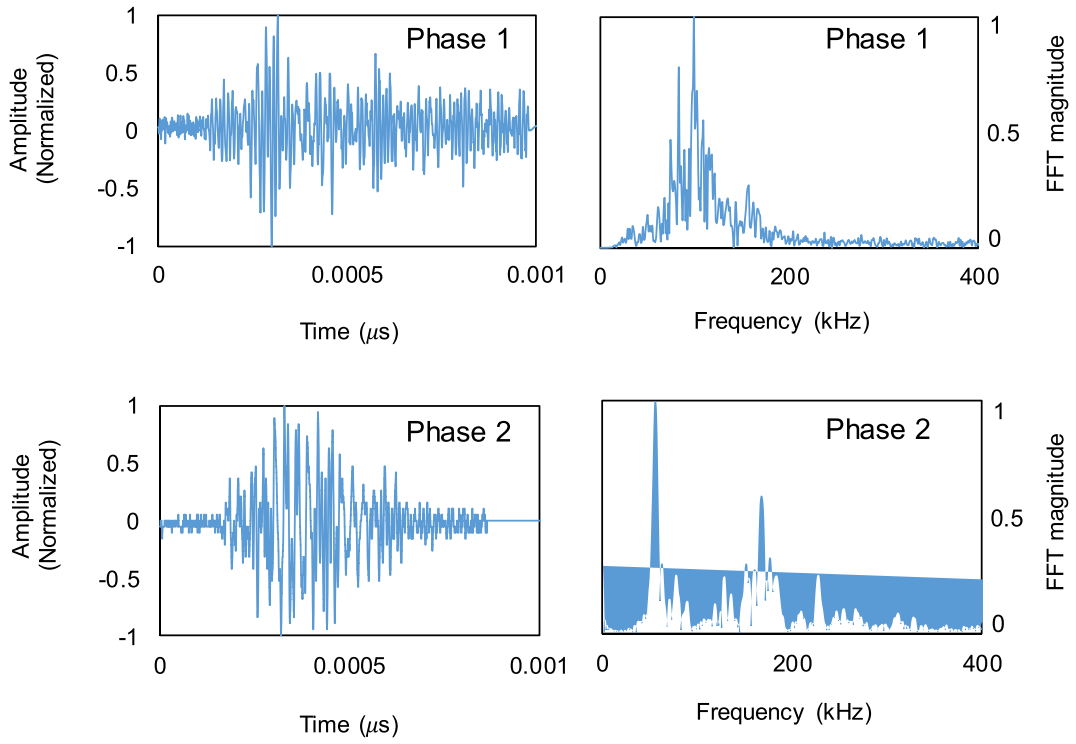

Fig. 7. Waveforms of AE signals in Phase 1 and 2.

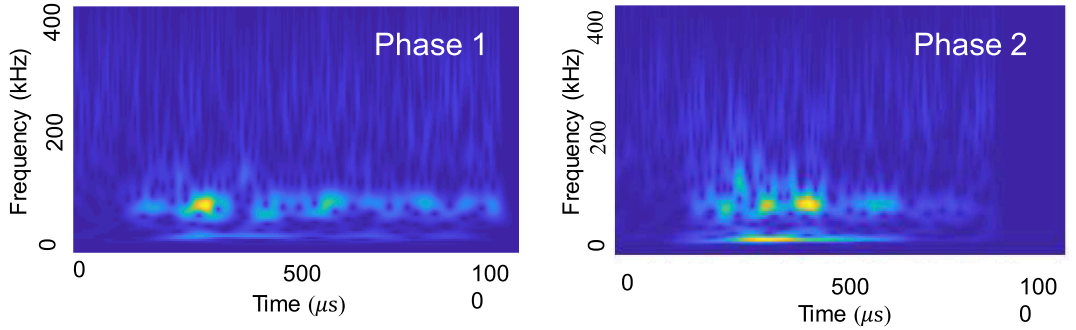

(a) Phase 1 (b) Phase 2

Fig. 8. CWT image of AE signals in class 1 and 2.

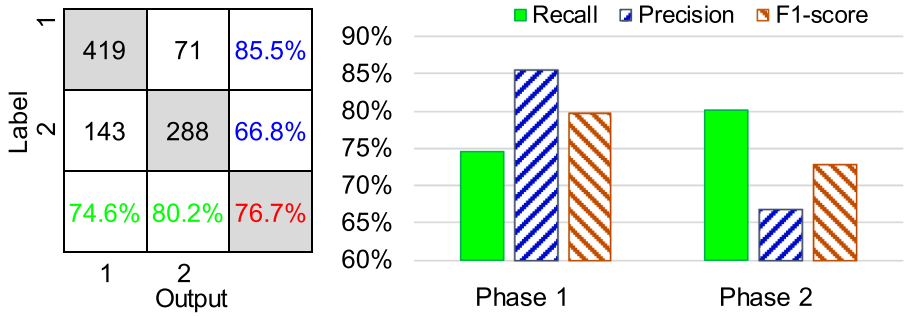

(a) Confusion matrix (b) Recall, precision, and F1-score

Fig. 9. Performance of CNN using all AE signals:

parameter of the CNN model for classes 1 and 2 was calculated as 74.6% and 80.2% (Fig. 9a).

The precision parameter has an inverse relationship with the recall parameter. Generally, a class with a high precision value has a low recall value and vice versa (Buckland and Gey, 1994). F1-score is a parameter to evaluate the efficiency of the classifier in each phase (class) by considering both recall and precision parameters. The F1-score is the harmonic mean of the precision and recall (Zhong et al., 2019). The values of the F1-score for phase 1 and phase 2 are 79.7% and 72.9%, respectively, and presented in Fig. 9b.

4.3.2. Classification using AE signals recorded by a single sensor

A CNN model was developed using the data from one sensor. The selected sensor (sensor 6) had the largest number of AE signals (421) among all sensors. AE signals were transferred to CWT images. Among all images, 70% of the data were randomly selected for the training set, and the rest (30%) were employed for the validation set. The result of the CNN model is presented in Fig. 10a. Among the images in phase 1, 85.5% of images were correctly classified as phase 1, and 14.5% of images were misclassified as phase 2. Among the images in phase 2, 86.0% of images in phase 2 were successfully classified, and 14.0% of images were erroneously assigned to phase 1. The total accuracy of the model is 85.7% (Fig. 10a). The precisions of phases 1 and 2 are 90.2% and 79.6%, respectively (Fig. 10a). The recall parameters for phases 1 and 2 are 85.5% and 86.0%, respectively (Fig. 10a). The F1-score for phases 1 and 2 are 87.8% and 82.7%, respectively (Fig. 10b).

4.4. Evaluation of ASR using stacked autoencoder

The FFT magnitudes of AE signals were employed as the input for the stacked autoencoder models. The ratios of training and validation data for the autoencoder models were consistent with the selected ratios for CNN models. The assigned classes (phases) for the AE signals were utilized as the data labels, similar to the CNN models. The results are presented in Fig. 11. The accuracy of classification using all signals is 72.6%. The precision parameters for phases 1 and 2 are 76.1% and 68.4%, respectively. The recall parameter for phases 1 and 2 are 74.6% and 70.1%, respectively (Fig. 11a). The F1-score parameter for phases 1 and 2 are 75.4% and 69.2%, respectively (Fig. 11b). The total accuracy of classification for the autoencoder model using signals from a single sensor is 80.2%. The precision values for phases 1 and 2 are 87.8% and 61.1%, respectively. The recall values of phases 1 and 2 are 84.9% and 66.7%, respectively (Fig. 11c). The F1-score values for phases 1 and 2 are 86.3% and 66.4%, respectively (Fig. 11d).

4.5. Comparison and discussion

Two shallow machine learning methods, Support Vector Machine (SVM) and K-Nearest Neighbor (KNN) were also utilized to correlate AE signals to ASR expansion, and the results were compared with the deep learning models. The input data of the machine learning models are the parametric features extracted from the AE waveforms. The names of the features and their description are presented in Table 1. According to the accuracies observed in CNN and stacked autoencoder, the model trained by signals from a single sensor indicated a higher accuracy than the models using all signals. Therefore, in this paper, the SVM and KNN models were trained and tested by the signal features from the single sensor.

In this paper, the RBF was selected as the kernel function of SVM (Scholkopf et al., 1997). The "K" for the KNN model was set to 4 after conducting serval trial and error tests. The classification accuracies of CNN, stacked autoencoder, SVM, and KNN are presented in Table 2. The CNN models have higher classification accuracies than the autoencoder model, and the deep learning methods have higher accuracies than the two shallow machine learning methods. The accuracy of the CNN model using the data from a single sensor is the highest among the evaluated methods (85.2%). Computing time is evaluated for the models. The average time required for training and the average time to classify a single signal in the test dataset are presented in Table 2. The training time for CNN process (using GPU-GTX-1080) is significantly more than the training times for the other models using intel i7-6700 CPU. However, the times for the trained models to classify a single AE signal are almost similar, as shown in Table 2. All the trained models can finish their task within 0.1 s. For the application envisioned, the model will be trained offline; therefore, the training time will not be a primary concern.

The F1-scores parameters for the four proposed models are presented in Fig. 12. F1-score values of the CNN model using data from the single sensor are generally the highest, and they are relatively consistent between the two classes (Fig. 12). However, a notable difference of F1-scores in the two classes can be observed in the autoencoder models (Fig. 12).

The CNN model using data from the single sensor has the highest accuracy and the most consistent performance among the two classes. Therefore, the CNN model is a better option to estimate the range of ASR volumetric strains from AE signals than the autoencoder models.

5. Summary and conclusions

The evaluation method based on deep learning is proposed to assess the condition of ASR progress in concrete structures. To verify the effectiveness of the proposed method, a concrete specimen with reactive coarse and reinforcements was cast and placed in a chamber for 300 days to accelerate the ASR by providing high temperature and humidity. AE sensors were affixed on the specimen surfaces to acquire stress waves emitted during the ASR due to cracking. The ASR expansion was

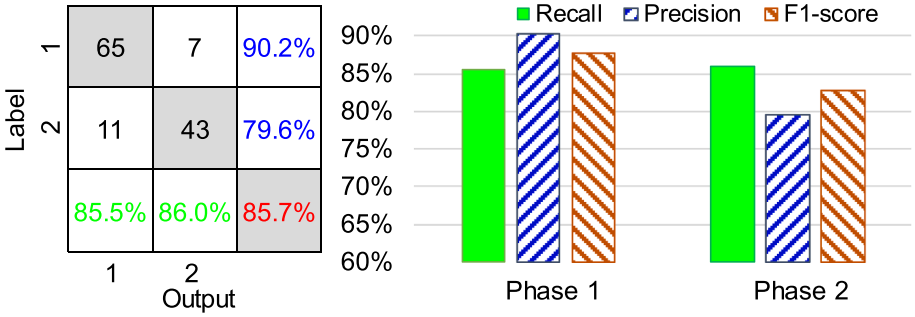

(a) Confusion matrix (b) Recall, precision, and F1-score

Fig. 10. Performance of CNN model using data from a single sensor.

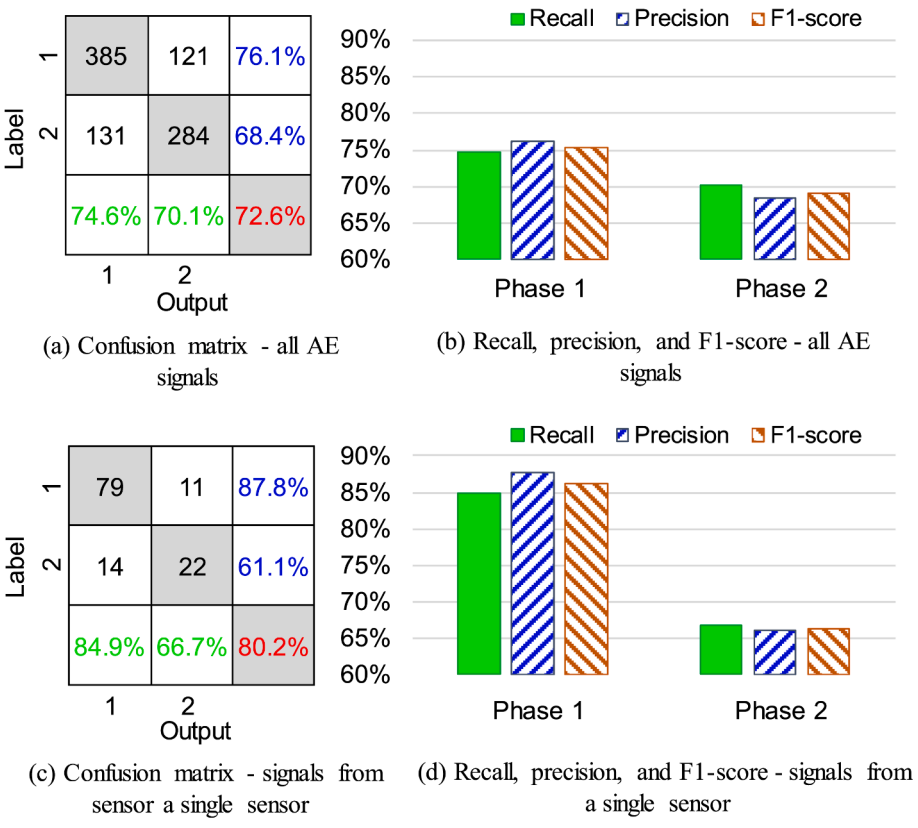

(a) Confusion matrix - all AE signals

(b) Recall, precision, and F1-score - all AE signals

(c) Confusion matrix - signals from sensor a single sensor

(d) Recall, precision, and F1-score - signals from a single sensor

Fig. 11. Performance of stacked autoencoder.

Table 1
Descriptions of the input parametric features.

Parametric features	Feature descriptions
Amplitude Energy	The peak amplitude of AE waveform The measure of the electrical energy measured for an AE signal
Count Counts to peak (PCNTS)	The number of threshold crossings The number of threshold crossings from the first threshold crossing to the peak
Rise time	The time interval between first threshold crossing and peak
Duration	The time between the first and last threshold crossing
Average frequency Signal strength	Counts divided by Duration A parameter to characterize the overall frequency content of an AE signal
Absolute energy	The absolute measure of the electrical energy measured for an AE signal
Peak frequency	Frequency of maximum signal contribution
Reverberation frequency	Frequency after the peak
Initial frequency	Frequency before the peak
Signal strength	Integral of the rectified voltage signal over the duration of the AE waveform

Table 2
Accuracies and computing times of all the models.

Models	Accuracy	Training Time (s)	Testing time (s)	Platform
Stacked autoencoder (all signals)	72.6%	377.64	0.04	CPU i7-6700
Stacked autoencoder (signals from a single sensor)	80.2%	219.57	0.03	CPU i7-6700
CNN (all signals)	76.7%	1562.12	0.08	GPU GTX1080
CNN (signals from a single sensor)	85.2%	612.36	0.06	GPU GTX1080
SVM (features from a single sensor)	71.2%	2.51	0.01	CPU i7-6700
KNN (features from a single sensor)	69.2%	1.64	0.01	CPU i7-6700

measured using DEMEC gauge on a regular basis. A CNN and stacked autoencoder models were trained using the AE data for classification purposes and determining ASR volumetric strain ranges. The main conclusions of the paper are summarized as follows:

- Both CNN and stacked autoencoder can classify the AE signals to their ASR phases with acceptable accuracy, while a higher accuracy was observed in the classification using the CNN than stacked autoencoder. In addition, using AE signals from a single sensor leads to a better performance of classification than using signals captured by all the sensors.
- The F1-scores indicated that the classification result of CNN using signals from a single sensor has the best performance in both phases (classes). Moreover, good consistency of F1-scores between two phases was observed for the CNN models.
- Considering computing time, global accuracy, and classifier performance in two phases, the CNN model using the data from a single sensor is the most efficient model among the evaluated models to monitor the temporal evolution of the concrete specimen affected by ASR.

ASR data accessibility for real concrete structures is one of the practical issues for training a supervised learning method. Future research could focus on either the novel AE data augmentation method or utilizing a numerical model to generate sufficient training data.

6. Data availability

The raw/processed data required to reproduce these findings can be

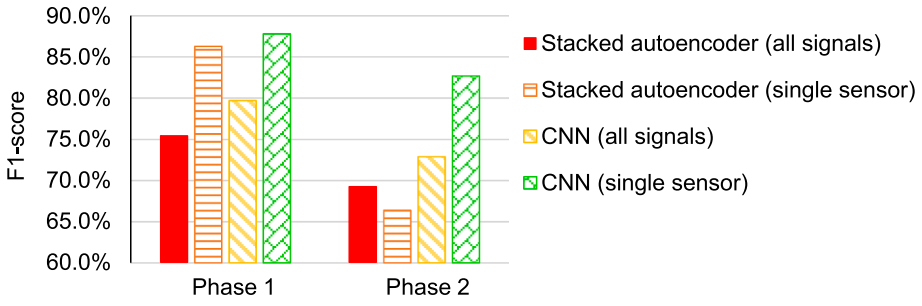

Fig. 12. F1-score of phases 1 and phase 2.

made available upon request and with the written permission of the sponsor.

CRediT authorship contribution statement

Li Ai: Conceptualization, Methodology, Formal analysis, Investigation, Writing - original draft. **Vafa Soltangharaei:** Conceptualization, Methodology, Formal analysis, Investigation, Writing - original draft. **Paul Ziehl:** Conceptualization, Methodology, Supervision.

Declaration of Competing Interest

The authors declare that they have no known competing financial interests or personal relationships that could have appeared to influence the work reported in this paper.

Acknowledgments

This research was partially supported by the U.S Department of Energy-Nuclear Energy University Program (NEUP) under the contract DE-NE0008544 and the U.S. Department of Energy Office of Science, Office of Basic Energy Sciences and Office of Biological and Environmental Research under Award Number DE-SC-00012530.

References

Abdelrahman, M., ElBatanouny, M.K., Ziehl, P., Fasl, J., Larosche, C.J., Fraczek, J., 2015. Classification of alkali–silica reaction damage using acoustic emission: A proof-of-concept study. Constr. Build. Mater. 95, 406–413.

Ai, L., Soltangharaei, V., Bayat, M., Greer, B., Ziehl, P., 2021a. Source localization on large-scale canisters for used nuclear fuel storage using optimal number of acoustic emission sensors. Nucl. Eng. Des. 375, 111097.

Ai, L.i., Soltangharaei, V., Bayat, M., Van Tooren, M., Ziehl, P., 2021b. Detection of impact on aircraft composite structure using machine learning techniques. Meas. Sci. Technol. 32 (8), 084013. https://doi.org/10.1088/1361-6501/abe790.

Anay, R., Lane, A., Jáuregui, D.V., Weldon, B.D., Soltangharaei, V., Ziehl, P., 2020. On-Site Acoustic-Emission Monitoring for a Prestressed Concrete BT-54 AASHTO Girder Bridge. J. Perform. Constr. Facil 34 (3), 04020034.

Anay, R., Soltangharaei, V., Assi, L., DeVol, T., Ziehl, P., 2018. Identification of damage mechanisms in cement paste based on acoustic emission. Constr. Build. Mater. 164, 286–296.

Assi, L., Soltangharaei, V., Anay, R., Ziehl, P., Matta, F., 2018. Unsupervised and supervised pattern recognition of acoustic emission signals during early hydration of Portland cement paste. Cem. Concr. Res. 103, 216–225.

Bach, F., Thorsen, T.S., Nielsen, M., 1993. Load-carrying capacity of structural members subjected to alkali-silica reactions. Constr. Build. Mater. 7 (2), 109–115.

Bakker, J. 2008. Control of ASR related risks in the Netherlands. In: Proceedings of the 13th International Conference on Alkali-Aggregate Reaction in Concrete, Trondheim, Norway.

Bengio, Y., Lamblin, P., Popovici, D., Larochelle, H., 2007. Greedy layer-wise training of deep networks. In: Advances in neural information processing systems.

Buckland, M., Gey, F., 1994. The relationship between recall and precision. J. Am. Soc. Informat. Sci. 45 (1), 12–19.

Campos, A., Lopez, C.M., Blanco, A., Aguado, A., 2018. Effects of an internal sulfate attack and an alkali-aggregate reaction in a concrete dam. Constr. Build. Mater. 166, 668–683.

Clark, L. 1989. Critical review of the structural implications of the alkali silica reaction in concrete: Bridges Design, Structures Group, Transportation andRoad Research Laboratory.

Deng, J., Dong, W., Socher, R., Li, L.-J., Li, K.,Fei-Fei, L. 2009. Imagenet: A large-scale hierarchical image database. In: 2009 IEEE conference on computer vision and pattern recognition.

Ebrahimkhanlou, A., Dubuc, B., Salamone, S., 2019. A generalizable deep learning framework for localizing and characterizing acoustic emission sources in riveted metallic panels. Mech. Syst. Sig. Process. 130, 248–272.

Farnam, Y., Geiker, M.R., Bentz, D., Weiss, J., 2015. Acoustic emission waveform characterization of crack origin and mode in fractured and ASR damaged concrete. Cem. Concr. Compos. 60, 135–145.

Goodfellow, I., Bengio, Y., Courville, A., Bengio, Y., 2016. Deep learning, (Vol. 1):. MIT press Cambridge.

Gou, L., Li, H., Zheng, H., Li, H.,Pei, X. 2020. Aeroengine Control System Sensor Fault Diagnosis Based on CWT and CNN. Mathemat. Probl. Eng., 2020.

Guo, F., Qian, Y., Wu, Y., Leng, Z., Yu, H., 2021. Automatic railroad track components inspection using real-time instance segmentation. Comput.-Aided Civ. Infrastruct. Eng. 36 (3), 362–377.

König, F., Jacobs, G., Stratmann, A.,Cornel, D. 2021a. Fault detection for sliding bearings using acoustic emission signals and machine learning methods. In: IOP Conference Series: Materials Science and Engineering.

König, F., Sous, C., Chaib, A.O., Jacobs, G., 2021b. Machine learning based anomaly detection and classification of acoustic emission events for wear monitoring in sliding bearing systems. Tribol. Int. 155, 106811.

Khan, A., Sohail, A., Zahoora, U., Qureshi, A.S., 2020. A survey of the recent architectures of deep convolutional neural networks. Artif. Intell. Rev. 53 (8), 5455–5516.

Kim, T.-Y., Cho, S.-B., 2019. Predicting residential energy consumption using CNN-LSTM neural networks. Energy 182, 72–81.

Krizhevsky, A., Sutskever, I.,Hinton, G. E. 2012. Imagenet classification with deep convolutional neural networks. In: Advances in neural information processing systems.

Li, D., Kuang, K.S.C., Koh, C.G., 2017. Fatigue crack sizing in rail steel using crack closure-induced acoustic emission waves. Meas. Sci. Technol. 28 (6), 065601.

Li, D., Kuang, K.S.C., Koh, C.G., 2018. Rail crack monitoring based on Tsallis synchrosqueezed wavelet entropy of acoustic emission signals: A field study. Struct. Health Monitor. 17 (6), 1410–1424.

Li, D., Wang, Y., Yan, W.-J., Ren, W.-X., 2020. Acoustic emission wave classification for rail crack monitoring based on synchrosqueezed wavelet transform and multi-branch convolutional neural network. Struct. Health Monitor. 1475921720922797.

Lilly, J.M., Olhede, S.C., 2008. Higher-order properties of analytic wavelets. IEEE Trans. Signal Process. 57 (1), 146–160.

Lokajíček, T., Přikryl, R., Šachlová, Š., Kuchařová, A., 2017. Acoustic emission monitoring of crack formation during alkali silica reactivity accelerated mortar bar test. Eng. Geol. 220, 175–182.

Ng, A.,Autoencoder, S. 2011. CS294A Lecture notes. Dosegljivo: https://web. stanford. edu/class/cs294a/sparseAutoencoder_2011new. pdf.[Dostopano 20. 7. 2016].

Niu, X.-X., Suen, C.Y., 2012. A novel hybrid CNN–SVM classifier for recognizing handwritten digits. Pattern Recogn. 45 (4), 1318–1325.

Ono, K., 2011. Application of acoustic emission for structure diagnosis. Diagnostyka 3–18.

Plusquellec, G., Geiker, M.R., Lindgård, J., De Weerdt, K., 2018. Determining the free alkali metal content in concrete–Case study of an ASR-affected dam. Cem. Concr. Res. 105, 111–125.

Rajabipour, F., Giannini, E., Dunant, C., Ideker, J.H., Thomas, M.D., 2015. Alkali–silica reaction: current understanding of the reaction mechanisms and the knowledge gaps. Cem. Concr. Res. 76, 130–146.

Redmon, J.,Farhadi, A. 2018. Yolov3: An incremental improvement. arXiv preprint arXiv:1804.02767.

Ren, S., He, K., Girshick, R., Sun, J., 2016. Faster R-CNN: towards real-time object detection with region proposal networks. IEEE Trans. Pattern Anal. Mach. Intell. 39 (6), 1137–1149.

Sadoughi, M., Downey, A., Bunge, G., Ranawat, A., Hu, C.,Laflamme, S. 2018. A deep learning-based approach for fault diagnosis of roller element bearings.

Saouma, V.E., Hariri-Ardebili, M.A., 2014. A proposed aging management program for alkali silica reactions in a nuclear power plant. Nucl. Eng. Des. 277, 248–264.

Schmidt, J.W., Hansen, S.G., Barbosa, R.A., Henriksen, A., 2014. Novel shear capacity testing of ASR damaged full scale concrete bridge. Eng. Struct. 79, 365–374.

Scholkopf, B., Sung, K.-K., Burges, C.J., Girosi, F., Niyogi, P., Poggio, T., Vapnik, V., 1997. Comparing support vector machines with Gaussian kernels to radial basis function classifiers. IEEE Trans. Signal Process. 45 (11), 2758–2765.

Shevchik, S.A., Kenel, C., Leinenbach, C., Wasmer, K., 2018. Acoustic emission for in situ quality monitoring in additive manufacturing using spectral convolutional neural networks. Addit. Manuf. 21, 598–604.

Soltangharaei, V., Anay, R., Ai, L., Giannini, E.R., Zhu, J., Ziehl, P., 2020a. Temporal Evaluation of ASR Cracking in Concrete Specimens Using Acoustic Emission. J. Mater. Civ. Eng. 32 (10), 04020285.

Soltangharaei, V., Anay, R., Assi, L., Ziehl, P., Matta, F., 2018a. Damage identification in cement paste amended with carbon nanotubes. In: AIP Conference Proceedings.

Soltangharaei, V., Anay, R., Hayes, N.W., Assi, L., Le Pape, Y., Ma, Z.J., Ziehl, P., 2018b. Damage mechanism evaluation of large-scale concrete structures affected by alkali-silica reaction using acoustic emission. Appl. Sci. 8 (11), 2148.

Soltangharaei, V., Hill, J., Ai, L., Anay, R., Greer, B., Bayat, M., Ziehl, P., 2020b. Acoustic emission technique to identify stress corrosion cracking damage. Struct. Eng. Mechan. 75 (6), 723–736.

Sun, R., Chen, Y., Dubey, A., Pugliese, P., 2021. Hybrid electric buses fuel consumption prediction based on real-world driving data. Transportat. Res. Part D: Transport Environ. 91, 102637.

Sun, Y., Zhang, H., Zhao, T., Zou, Z., Shen, B., Yang, L., 2020. A New Convolutional Neural Network With Random Forest Method for Hydrogen Sensor Fault Diagnosis. IEEE Access 8, 85421–85430.

Szegedy, C., Liu, W., Jia, Y., Sermanet, P., Reed, S., Anguelov, D., Rabinovich, A., 2015. Going deeper with convolutions. In: Proceedings of the IEEE conference on computer vision and pattern recognition.

Takakura, T., Mitsuki, S., Takiguchi, K., Nishiguchi, I., Ishikawa, T., Matsumoto, N., Masuda, Y. 2005. Investigation on the expansion value of turbine generator foundation affected by alkali-silica reaction.

Tcherner, J.,Aziz, T. S. 2009. Effects of AAR on seismic assessment of nuclear power plants for life extensions.

Weise, F., Voland, K., Pirskawetz, S., Meinel, D., 2012. Innovative measurement techniques for characterising internal damage processes in concrete due to ASR. University of Texas, Austin, TX, USA.

Xin, H., Cheng, L., Diender, R., Veljkovic, M., 2020. Fracture acoustic emission signals identification of stay cables in bridge engineering application using deep transfer learning and wavelet analysis. Advan. Bridge Eng. 1 (1), 1–16.

Zhong, L., Hu, L., Zhou, H., 2019. Deep learning based multi-temporal crop classification. Remote Sens. Environ. 221, 430–443.